ACS OMEGA

http://pubs.acs.org/journal/acsodf

Article

Prediction of Newtonian Droplet Breaking Time from a Capillary at Low Weber Numbers

Peifeng Lin,* Qi Chen, Youju Liu, Xiao Hu, and Zuchao Zhu

Cite This: *ACS Omega* 2022, 7, 23890−23898

Read Online

ACCESS | Metrics & More | Article Recommendations

ABSTRACT: Droplet formation and growth processes have numerous scientific and industrial applications. Experimental and numerical studies on the formation, growth, and breaking of droplet are carried out in present work. The numerical results are in good agreement with the experiment. This work focused on the effect of different Weber numbers (We) on the droplet breaking time. The results show when $We < 0.05$, the length and volume of the droplet increase, and the breaking time decreases rapidly. The resultant force acting on the main droplet suddenly drops around the critical breaking time. The difference rate between the time t_n (when the resultant force is zero) and the breaking time t_b is less than 8.49%. For the dimensional analysis of the numerical results, a prediction formula of breaking time on the Weber number is modeled as $aWe^b + c$ for $We < 0.5$.

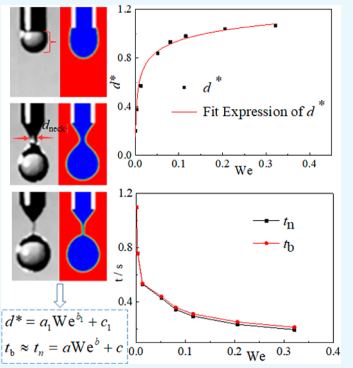

1. INTRODUCTION

Droplet formation is a quite common phenomenon in daily life, scientific research, and industrial production, such as inkjet printing, biomedicine, and petrochemical processing, and so forth. It is a tough task to understand the dynamics process of droplet formation through a capillary at a low Weber number (We), especially to predict the breaking time of the droplet. A vast amount of experimental and numerical investigations about the kinematic parameters, including the number, diameter and shape of the droplets, and dynamic factors, including the liquid viscosity and flow rate in the droplet formation, have been carried out in recent decades.

Nazari et al.[1] used a high-speed photographic system to obtain images of droplet evolution and analyzed the different droplet formation processes. The influence parameters of the primary droplets and satellite droplets were studied by Wang,[2] including liquid viscosity, flow rate, the ratio of capillary internal and external diameter, surfactant, and other influence factors. Liu et al.[3] carried out a detailed study on the shape change of droplet flow, and quantitative analyses about the necking process under different flow rates and tube diameters were discussed. An experimental study of water droplet formation was carried out by Brenner et al.,[4] and they drew a systematic conclusion on the formation process and dynamic characteristics in the stages of water droplet before and after breaking. The behavior of droplet in different forming stages was studied by changing fluid parameters.[5,6] Tang et al.[7] studied the effect of liquid viscosity on droplet shape by experiments. It is found that viscosity has a significant effect on droplet shape and length. The micro thread is formed between the droplet and the remainder as the droplet to individual droplet, which is more obvious at high viscosity. Dastyar et al.[8] conducted experiments to understand the physical and geometric parameters of droplet formation, and the effects of the surfactant concentration on droplet elongation, minimum neck thickness, formation time, and droplet volume were revealed. The main stages of drop on demand (DOD) drop formation, including injection and stretching of liquid, pinch-off of liquid thread from the nozzle exit, droplet shrinkage, breakup of liquid thread into primary droplet and satellites, and recombination of primary droplet and satellites, are analyzed based on the experimental results.[9] Zhang et al.[10] experimentally analyzed that when the flow rate was low enough, the droplets were injected out of the nozzle in a discrete and uniform manner.

Even though many experimental studies on droplet formation have been carried out, the complete mechanism under the process is still not well understood due to the insufficiency of the experimental data. In the past decades, computational fluid dynamics simulation has developed vigorously, which has gradually become a powerful tool for analyzing complex interphase coupling problem.[11] The process of liquid outflows through the capillary, which is governed by

Received: April 27, 2022
Accepted: June 17, 2022
Published: June 28, 2022

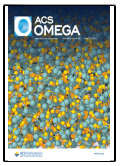

https://doi.org/10.1021/acsomega.2c02602
ACS Omega 2022, 7, 23890−23898

the Navier−Stokes equation, and forms a droplet that can be considered as an axisymmetric flow; thus, a cylindrical coordinate is usually adopted, and the three-dimensional model can be simplified to a two-dimensional model in most cases. From this fundamental assumption, many improvements of the simulation method have been published. Ambravaneswaran et al.[12] proposed a two-dimensional finite element method for obtaining droplet formation characteristics such as droplet volume and total streamline length. Eggers et al.[13] used Taylor expansion to simplify the two-dimensional model to obtain a one-dimensional finite element model. Subramani et al.[14] studied the relation between Weber number, Ohnesorge number, gravity bond number, and flow state by combination of the experiment, high-speed imaging, and computation, in which the one-dimensional slender-jet equations are solved numerically by finite element analysis. Xu et al.[15] used numerical simulation to both advance the mechanistic understanding of interface pinch-off in DOD droplet formation and develop insights into the effects of the governing dimensionless groups on the underlying dynamics. Some scholars presented a complementary experimental and computational investigation, such as the effect of viscosity and flow rate on the dynamics of droplet formation in the dripping mode.[16−23]

In summary, a lot of studies have been carried out about the droplet formation process based on experimental and numerical methods. However, most of these studies focus on the droplets themselves in the core flow range of the dripping region and less on the interactions between the droplets and the peripheral devices, which will rise to become the main issue in some special applications, such as the inkjet printing applications, desulfurization solidification in the petrochemical industry, and accurate control of the droplet spreading onto a basal plate. The interactions will be significantly influenced by both the terminal axial velocity and the breaking time of the droplet, especially at the flow conditions in the transition region from dripping to jetting. In this work, we consciously chosen parameters close to the critical flow value. In our previously estimation study, the result flow pattern under the transition condition is combined dripping and jetting, which is a main drop followed by a jetting column. The work was mainly emphasized on the analysis of the droplet breaking time at low Weber numbers (but cover the whole dripping region) through experiments and numerical simulations. Variation of the geometric characteristics parameters, such as limiting lengths of droplets and primary droplet volume, contact angle (angle between the interface and the tip of a capillary wall), and average droplet growth velocity were analyzed. Finally, the flow Weber numbers are used to represent the breaking time and droplet neck diameter as a function, respectively.

2. MATHEMATICAL FORMULATION AND NUMERICAL ANALYSIS

2.1. Governing Equations. In this work, the flow is assumed to be an incompressible glycerin and air two-phase flow. The droplet formation is simulated by solving a set of conservation equations, which are decided by the volume fractions of all phases with different property ρ and μ. The equations are as follows:

Equation of continuity

$$\nabla\cdot\boldsymbol{v} = 0 \tag{1}$$

Equation of motion

$$\frac{\partial(\rho\boldsymbol{v})}{\partial t} + \nabla\cdot(\rho\boldsymbol{v}\otimes\boldsymbol{v}) = -\nabla P + \mu\nabla^2\boldsymbol{v} + \rho\boldsymbol{g} + \boldsymbol{F}_\sigma \tag{2}$$

where ρ is the liquid density, $\boldsymbol{v}$ is the velocity vector, P is the pressure, μ is the liquid dynamic viscosity, and $\boldsymbol{F}_\sigma$ is the surface force.

During the droplet formation, the interface between glycerin and air is captured and reconstructed by the volume of fluid (VOF) method. A schematic of the droplet formation is shown in Figure 1. Under the action of gravity, this study was

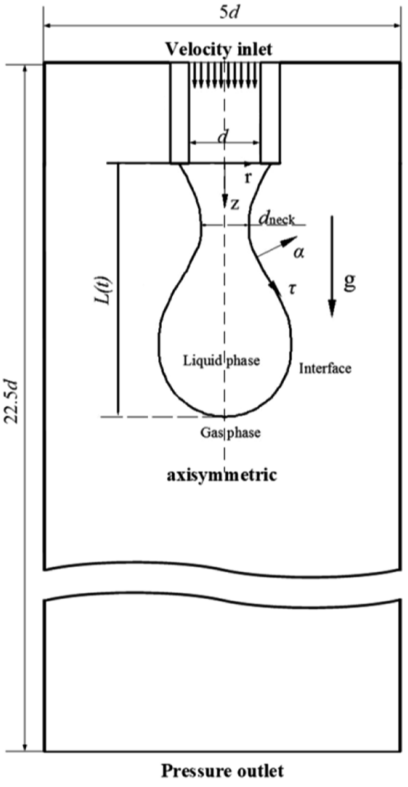

Figure 1. Schematic of vertical capillary droplet formation at constant flow.

simplified to a two-dimensional axisymmetric simulation via FLUENT 18.0. Mainly focusing on the deformation process, the meshes near the axis were refined, the simulation results were compared with the experimental results, and a suitable set of grids was finally selected for calculation. The boundary conditions are velocity inlet and pressure outlet. To deal with the velocity−pressure coupling, the PISO algorithm was used. To capture the free interface, the geometric reconstruction method based on piecewise−linear interface calculation was adopted. Compared with other interface reconstruction methods, this method is the most accurate and is more suitable for this work. Laminar flow was used in the simulation due to the small Reynolds number.[24]

For the qth phase, the control equation has the following form

$$\frac{\partial}{\partial t}(\alpha_q\rho_q) + \nabla\cdot(\alpha_q\rho_q\boldsymbol{v}_q) = S_{\alpha_q} \tag{3}$$

where α_q is the volume fraction of the q-phase, ρ_q is the density of the q-phase, $\boldsymbol{v}$ is the velocity vector of the q-phase, and S_{α_q} is the source phase, the value is 0.

https://doi.org/10.1021/acsomega.2c02602
ACS Omega 2022, 7, 23890−23898

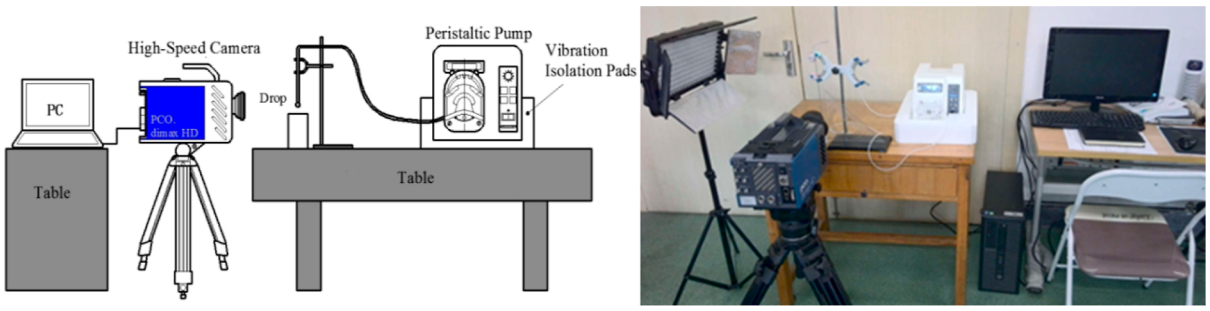

Figure 2. Schematic of the experimental setup.

Table 1. Physical Properties of Glycerol Solution

C	ρ (g/cm^3)	μ (g/cm s)	σ (N/m)	v (m/s)	Weber number
50% glycerol	1.225	0.061	0.07	0.005−0.1	0.0008−0.3211

Because of axisymmetric, the droplet shape must obey the following relation at the droplet tip

$$\boldsymbol{\tau}\cdot e_z = 0 \text{ at } r = 0,\ z = L(t) \text{ on } S(t) \tag{4}$$

where e_z is the unit vector in the z-direction and $L(t)$ is the instantaneous length of the droplet. The velocity decomposes on the tip of the capillary

$$v_r = 0,\ v_z = \text{const} \tag{5}$$

where v_r and v_z are the radial and axial components of the velocity, respectively. The initial condition is that the fluid is static, and the pressure of the entire fluid is constant at $t = 0$.

$$\boldsymbol{v}(0, r) = \mathbf{0},\ p(z, 0) = \text{const} \tag{6}$$

2.2. Analysis of the Forces in the Forming Process. The force analysis of the droplet in the forming process is quite complicated. According to the literature,[25,26] there are four main forces that affect the formation process. Wei and Ngan et al.[27] made a detailed description about the four forces: buoyancy (F_B), kinetic force (F_K), drag force (F_D), and surface force (F_σ) opposite to the direction of motion. In this work, the buoyancy force is negligible because of the relative low density of air, but droplet gravity is taken into account. Furthermore, both the Ohnesorge number ($Oh = \mu/(\rho d\sigma)^{1/2}$) and the Weber number($We = \rho v^2 d/\sigma$) are small, which means that the magnitude of viscous force and the drag force are small compared with the surface tension, so they can be ignored either. The force equilibrium between gravity and surface force is as follows

$$(F_G)_{whole} = (F_\sigma)_{vertical} \tag{7}$$

$$(F_G)_{whole} = \rho V_d g,\ (F_\sigma)_{vertical} = \pi d_{wetted}\sigma \sin\theta \tag{8}$$

where ρ is the liquid density, V_d is the whole droplet volume, g is the gravitational acceleration, d_{wetted} is the wetted diameter of the capillary, σ is the surface tension, and θ is the contact angle between the interface and the tip of the capillary wall. Due to droplet shape and wall wettability, the contact angle varies during the forming process rather than a fixed value, according to Byakova et al.[28]

3. EXPERIMENTAL APPARATUS AND SIMULATION VALIDATION

3.1. Experimental Apparatus. The formation process of droplet flowing into air at a constant flow rate from the tip of a vertical capillary was experimentally studied. As shown in Figure 2, the experimental scheme is composed of a stainless-steel capillary tube (outer diameter is 3 mm, and inner diameter d = 2 mm), a peristaltic pump, a high-speed camera, and other components. Stable and continuous flow is provided by the peristaltic pump (BT100-1F), and the flow rate range is 0.2 to 500 mL/min. The bottom of the peristaltic pump is involved in the treatment of anti-vibration to achieve a good effect of anti-vibration. Several sets of experiments were carried out, and it was found that the vibration had a little effect on the experimental results. The droplet formation sequence images are taken by a high-speed camera (PCO. dimax HD). It has an advanced Complementary Metal-Oxide Semiconductor (CMOS) sensor with a maximum resolution of 1920 × 1080 pixels. The highest recording rate used in this work is 2000 fps to capture the droplet breakup, and the scale of the sequence image was determined as 10.023 pixels/mm. The backlight is powered by a 500 W bulb. The properties of glycerin solution are shown in Table 1.

3.2. Simulation Validation. The geometry of the numerical simulation is consistent with the experiment. After the numerical simulation considering gravity and the surface tension, the droplet shape and necking length were captured by the geometric reconstruction method of VOF. As shown in Figure 3, the results of the experiment and simulation both show that the droplet formation process could be divided into three stages: forming stage, necking stage, and breaking stage

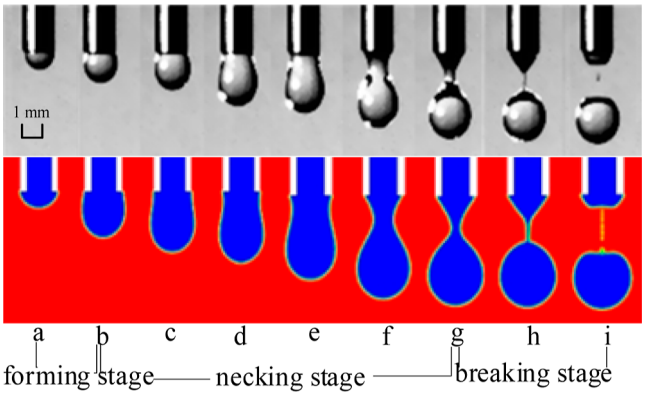

Figure 3. Comparison of the droplet formation process between experiment and simulation.

https://doi.org/10.1021/acsomega.2c02602
ACS Omega 2022, 7, 23890−23898

according to the appearance of the droplet necking. The length of the glycerol droplet with a velocity of v = 0.005 m/s and the mass fraction of 50% was compared between the experiment and simulation, as shown in Figure 4. The results show a good agreement with each other in every stage, and the simulation method can be validated.

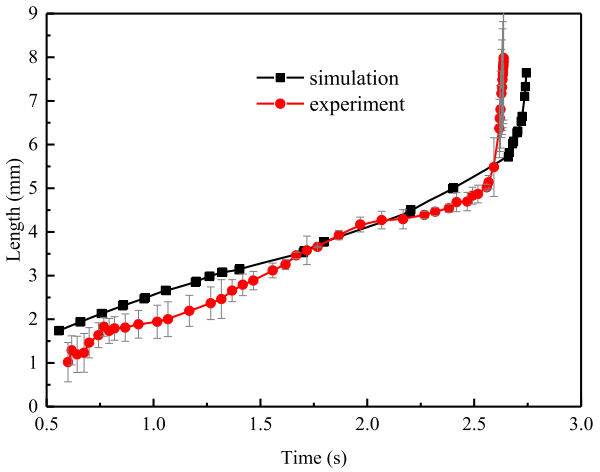

Figure 4. Comparison of the droplet formation length between experiment and simulation.

4. RESULTS AND DISCUSSION

Based on the numerical simulation, the axial velocity, the internal pressure of the droplet when it is formed, and the vortex outside the droplet were analyzed in the work. The changes in the geometric parameters in the three stages of droplet forming were drawn. According to the change in droplet volume and the force analysis of the droplet in the equilibrium state, the prediction function of the breaking time and neck diameter of the droplet were obtained.

4.1. Flow Evolution during the Droplet Formation.

Figure 5 shows the velocity of the glycerol-air two-phase flow.

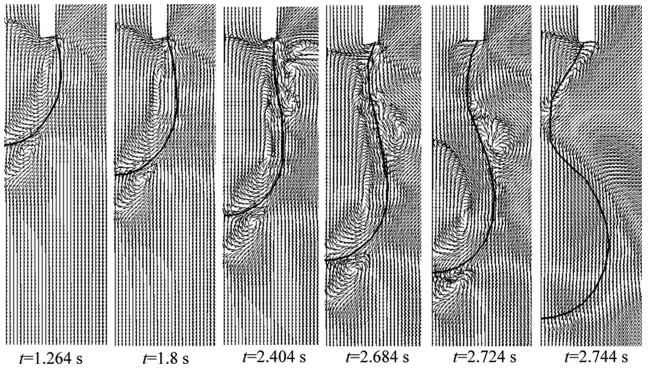

Figure 5. Velocity evolutions of the two-phase flow.

It can be seen that the velocity of the droplet tip increases with the growth of the droplet at 1.264 and 1.8 s. A clockwise vortex in the droplet is formed at the edge of the interface. As a result, the fluid at the centerline of the capillary outlet is pushed toward the outside. When the velocity increases, the air vortex outside the tip of the droplet also becomes larger. At 2.404 and 2.684 s, due to the increase in the volume of the droplet, the vortex is progressively stretched into a slender thread under the influence of gravity. At 2.724 s, due to the obvious necking phenomenon and the increase in the volume of the droplet, the much larger vortex appeared near the centerline of the droplet, which will further reduce the diameter of the droplet neck. The velocity near the contact point between the droplet and capillary begins to point from the outside to the center. At 2.744 s, the droplet is about to breakup, and the vortex in the droplet is dissipated due to the effect of viscosity. After the droplet is broken, the velocity direction of each point in a single droplet formed is the same, and the droplet falls down.

Figure 6 shows the variation of the axial velocity along the z-direction at different times. As shown in Figure 6a, there is a peak and a trough in the axial velocity, indicating that a vortex is generated. Combined with the previous results in Figure 5, due to the slow flow rate, the liquid at the nozzle is squeezed out, forming a vortex near the nozzle. As the liquid flows into the droplet, the position of the vortex moves toward the centerline. As the volume of the droplet increases, the increase in gravity causes the vortex to become larger, and the neck phenomenon occurs (as shown in Figure 6b). Due to the effect of gravity, the vortex appears in the liquid below the necking portion. At the breaking time 2.744 s, the axial velocity varies sharply, and the relative velocity difference reaches the maximum value, which will stretch and shrink the neck and finally cause the droplet breakup.

Figure 7 shows how the internal pressure contours change during the formation of droplets. It is evident from Figure 7a–d that the pressure at the tip of the droplet is larger than that near the nozzle outlet. At each time period, the pressure gradually increases from the inlet to the tip of the droplet, which is similar to the hydrostatic pressure distribution. It will stretch the droplet and increase the droplet volume. However, the liquid inside the droplet continues to flow through the pressure gradient due to inertia and gravity. It can be seen from Figure 7e that in the breaking stage, the neck becomes thinner sharply, and the pressure increases significantly to 360 Pa, which is significantly higher than the pressure near the top of the droplet and the nozzle. At this time, due to the existence of the pressure difference, the droplets below the necking tend to move downward under the action of the pressure difference. The conical part above the neck has a tendency to move upward, resulting in a narrowing of the diameter at the neck diameter. Finally, when the diameter of the necked portion approaches zero, the tensile stress on the radial cross-section of the droplet at the necked portion tends to infinity until the droplet finally breaks.

The different processes of droplet formation are shown in Figure 8. The contact angle is defined as the angle between the surface tangent and the horizontal dashed line. It represents the component of surface tension acting in the vertical direction opposite to the direction of droplet separation.

The change of droplet geometric parameters when v = 0.005 m/s is shown in Figure 8. Three stages of droplet formation were analyzed.

(1) Forming stage (0–0.46 s, as shown in Figure 9)

During this stage, the liquid flows out of the capillary, first forming a meniscus shape, and suspending on the wall of the capillary. The contact angle decreases sharply and reaches a critical value, as shown in Figure 9. The wetted diameter increases sharply and reaches a critical maximum (capillary outer diameter). The interface of line 1, as shown in Figure 8, is the situation when the liquid flows out from the inner wall of the capillary. As the droplet grows slowly, the wetted diameter

https://doi.org/10.1021/acsomega.2c02602
ACS Omega 2022, 7, 23890–23898

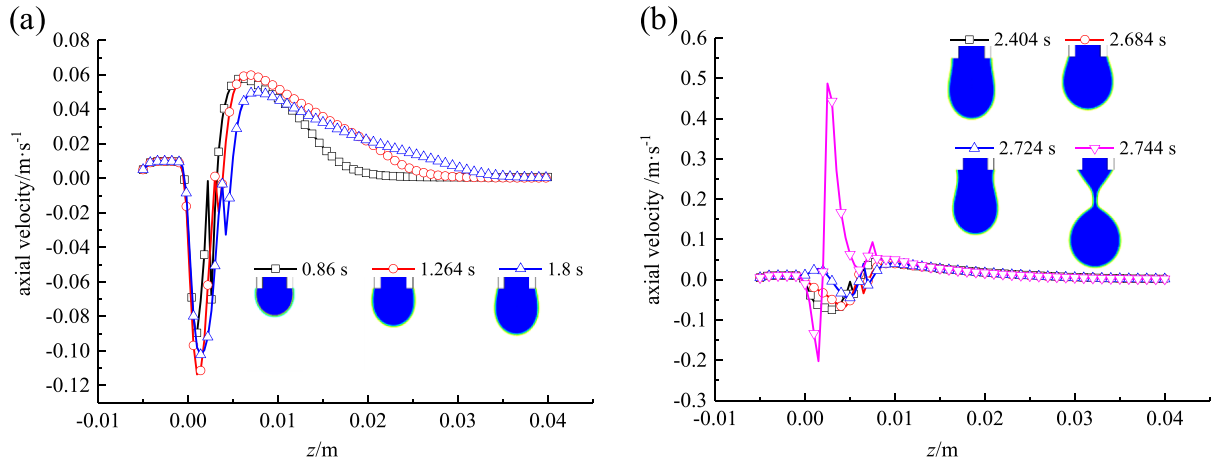

Figure 6. Variation of the axial velocity at different times. (a) t = 0.86 s, t = 1.264 s, and t = 1.8 s. (b) t = 2.404 s, t = 2.684 s, t = 2.724 s, and t = 2.744 s.

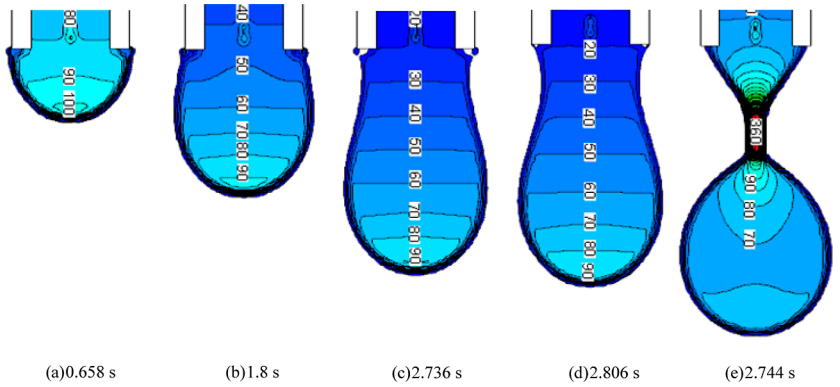

Figure 7. Variation of the internal pressure inside the droplet at different times.

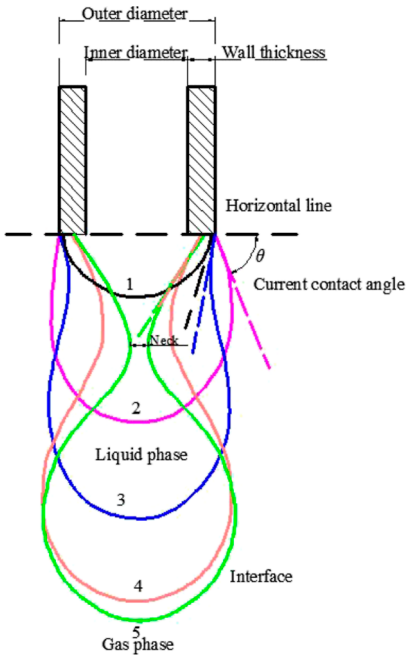

Figure 8. Schematic diagram of the different processes of droplet formation.

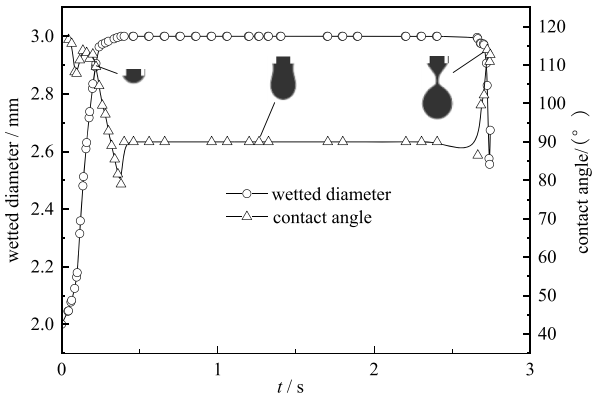

Figure 9. Changes in wetted diameter and contact angle (v = 0.005 m/s).

of the tip capillary wall increases. Due to the limited thickness of the capillary wall, the expansion of the meniscus is ended when it reaches the outer edge of the capillary, as shown by line 2 in Figure 8. When reaching the interface position of line 2, the droplet volume increases, and the wetted diameter reaches a fixed value.

(2) Necking stage (0.46−2.5 s, as shown in Figure 9)

During this stage, due to the inward contraction of the droplet, the shape of the droplet changes from a meniscus shape to an hourglass shape. The droplet is spherical from neck to its top, as shown by line 3 in Figure 8. The contact angle remains almost unchanged, and the wetting diameter remains at the constant value of the outer diameter of the capillary. As

https://doi.org/10.1021/acsomega.2c02602
ACS Omega 2022, 7, 23890−23898

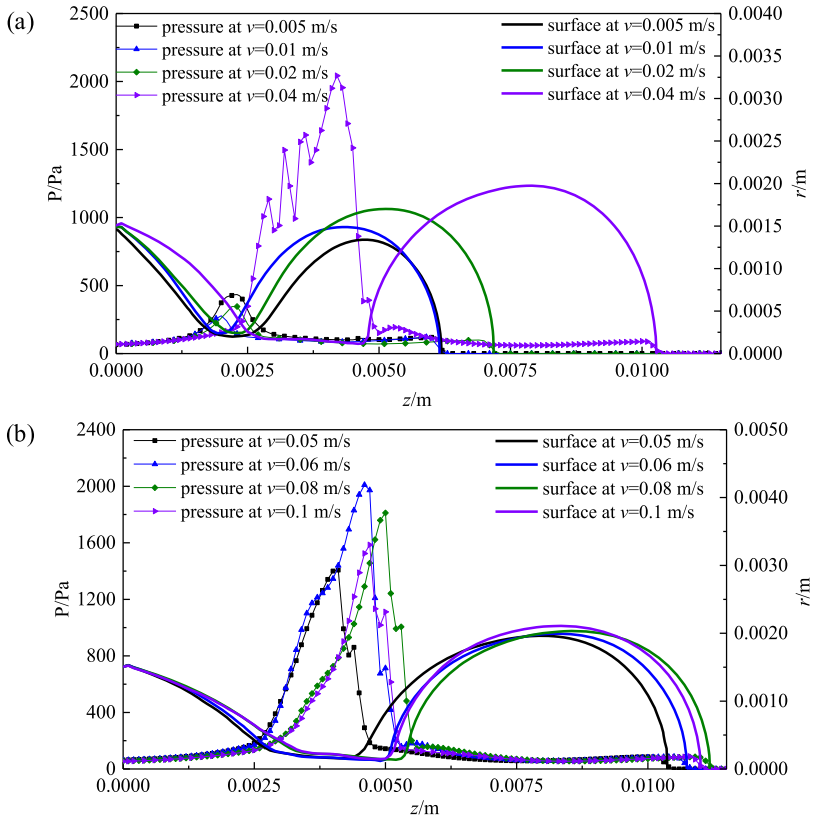

Figure 10. Static pressure on the axis at the time of fracture at different inflow velocities: (a) flow velocity is 0.005, 0.01, 0.02, and 0.04 m/s. (b) Flow velocity is 0.05, 0.06, 0.08, and 0.1 m/s.

the droplet volume gradually increases, the gravity of the droplet also increases.

(3) Breaking stage (2.5−2.744 s, as shown in Figure 9)

During this stage, there are significant changes in various parameters. As shown in Figure 9, when the contact angle is changed from 90 to 120°, the wetted diameter decreases. The capillary liquid falls into the primary droplet, forming interface lines 4 to 5, as shown in Figure 8. Gravity increases as the volume of the droplet increases, causing the droplet to breakup.

4.2. Effect of the Weber Number on the Droplet Formation. In order to understand the mechanism dominating the droplet breaking time, the forming process of droplets at different flow rates was numerically simulated, they were 0.005, 0.01, 0.02, 0.04, 0.05, 0.06, 0.08, and 0.1 m/s, respectively.

Figure 10 shows the variation of axial pressure at the breaking time with different inflow velocities. It can be seen from Figure 10a that the necking portion of the droplet is shorter at the flow rates of 0.005, 0.01, and 0.02 m/s, but the pressure fluctuation is not obvious at this time, and the axial pressure at the necking is the maximum value of 500 Pa. When the flow velocity changes from 0.02 to 0.04 m/s, the static pressure changes significantly. Because the necking portion of the droplet becomes longer, the pressure on the necking portion increases and fluctuates greatly, with a maximum of 2200 Pa. As shown in Figure 10b, the necking portion is longer when the flow velocity is 0.05, 0.06, 0.08, and 0.1 m/s, the pressure starts to increase from the beginning of the necking portion, the pressure reaches the maximum at the end of the necking portion, about 1800 Pa, and then, the pressure on the axis gradually decreases. Since the pressure at the neck is the largest, a pressure difference is formed at both ends of the necking portion, which makes the necking portion tend to move relative to each other. The necking portion becomes thinner and thinner, approaching zero, and the tensile stress on the radial section tends to infinity, which exceeds the critical tensile stress, so the droplet breaks.

As mentioned before, the Weber number ($We = \rho v^2 d/\sigma$), which represents the ratio of inertia force to surface force, varies with the inlet flow rate. Figure 11 shows the breakup time t_b (s) of the droplet, the length of the droplet at breakup L_b (mm), and the breakup volume V_b (10^{-8} m^3) as a function of the Weber number (We). It can be seen from the figure that

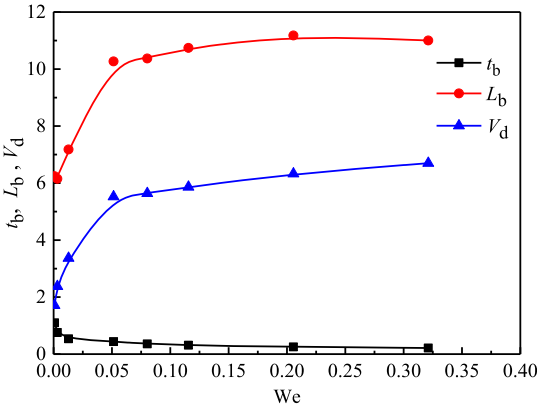

Figure 11. Breaking time, breaking length, and breaking volume at different Weber numbers.

https://doi.org/10.1021/acsomega.2c02602
ACS Omega 2022, 7, 23890−23898

when the Weber number is less than 0.05, the length and volume of the droplet increase more obviously than that when $We > 0.05$. Similar results can also be found for breaking time, which is when $We < 0.05$, the breaking time decreases rapidly with the increase in the Weber number.

The resultant force acting on the droplet is calculated by force analysis. It can be seen from Figure 12 that the resultant

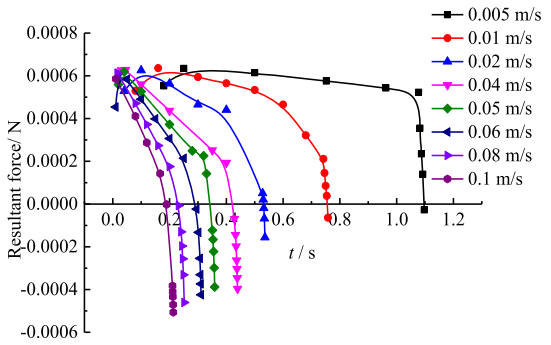

Figure 12. Resultant force during droplet formation at different flow rates.

force on the droplets slowly decreases with time at the growing and necking stage. Then, the resultant force suddenly drops, combined with the results shown in Figure 11, which is very close to the critical time for the droplet to breakup. As the velocity at the capillary increases, the time when the resultant force becomes zero is earlier. The slope of the resultant force line is also larger after the droplet force is balanced.

Inspired by the idea that the time when the resultant force is zero (t_n) can be the indicator of droplet breaking time (t_b), we compared their value at different Weber numbers, which is shown in Figure 13. It can be seen that the time t_n is very close

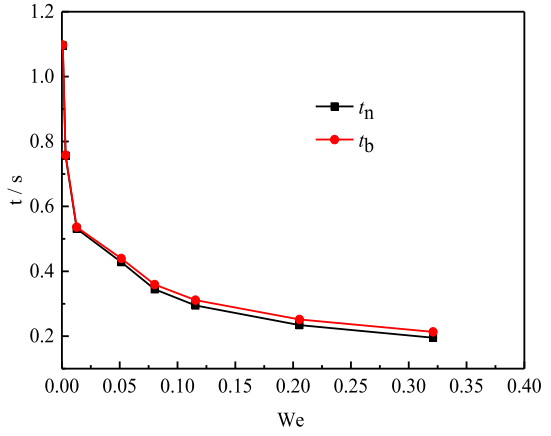

Figure 13. Breaking time and zero resultant force time at different Weber numbers.

to the breaking time at all flow rates. With the increase in Weber numbers, the difference between the time when the resultant force is zero and the breaking time increases slightly, with the difference rate from 0.15 to 8.49%, so the relationship between t_b and t_n can be approximately given as

$$t_b \approx t_n \tag{9}$$

4.3. Prediction of Droplet Neck Diameter. In order to predict the breaking time more reasonably, the droplet neck diameter was first investigated. The relationship between the

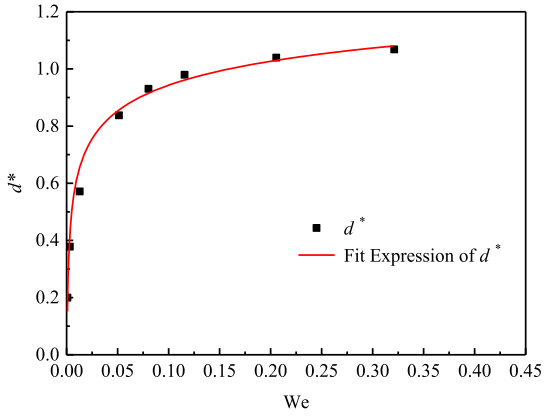

Figure 14. Relationship between dimensionless neck diameter and Weber number.

dimensionless neck diameter ($d^* = d_{neck}/d$) and We is shown in Figure 14. The fitting relationship between the two dimensionless numbers is

$$d^* = a_1 We^{b_1} + c_1 \tag{10}$$

where $a_1 = -0.916$, $b_1 = -0.107$, and $c_1 = 2.115$. Similarly, the relationship between V_d and V_n at zero resultant force time (t_n) is shown in Figure 15, where V_d is the whole droplet volume,

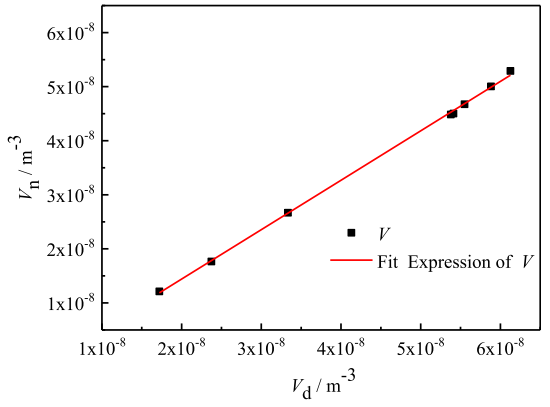

Figure 15. Relationship between the whole droplet volume V_d and the droplet volume below the neck V_n at zero resultant force time.

and V_n is the main droplet volume below the neck. It can be seen from Figure 15 that there is a good linear relationship between V_d and V_n, and the relation between the two variables is $V_n = b_2 V_d$, where $b_2 = 0.914$.

4.4. Prediction of Droplet Breaking Time. The surface and gravity force dominate the droplet formation. The smaller the neck diameter, the lower the surface force due to the smaller perimeter, but the greater the Laplace pressure due to the larger curvature. Gravity increases as the volume increases. It can be seen from the fact that the droplet is not broken from the nozzle but is broken from the neck when the necking phenomenon occurs. Different with eqs 7 and 8, for the main portion of the droplet underneath the neck, we have

$$F_G = \rho V_n g, \quad F_\sigma = \pi d_{neck} \sigma \tag{11}$$

https://doi.org/10.1021/acsomega.2c02602
ACS Omega 2022, 7, 23890−23898

where V_n is the droplet volume below the neck and d_{neck} is the neck diameter. At the neck, the surface force is in the vertical direction. Therefore, the resultant force is zero, which can prove that the gravity F_G is equal to the surface force F_σ

$$F_G = F_\sigma \tag{12}$$

$$\pi d_{neck}\sigma = \rho V_n g \tag{13}$$

Equation 13 shows that the breaking time t_b is related with the neck diameter d_{neck}, liquid density ρ, surface tension σ, and the droplet volume below the neck V_n, which is based on Figure 15, linearly related to the whole droplet volume V_d. From the mass conservation principle, the whole droplet volume V_d is the time function of inlet velocity v and inner diameter d. Thus, the functional relationship between all these parameters is

$$t_n = f(d_{neck}, \sigma, v, d, \rho) \tag{14}$$

After a dimensional analysis of these parameters in the function, the following dimensionless relationship is obtained

$$\frac{t_n}{dv^{-1}} = f_1\left(\frac{\sigma}{dv^2\rho}, \frac{d_{neck}}{d}\right)$$

$$t_n = d\sqrt{\frac{\rho d}{\sigma We}} f_1\left(\frac{1}{We}, d^*\right) = f_2\left(\frac{1}{We}, d^*\right) \tag{15}$$

where We is the Weber number and $d^*$is the dimensionless neck diameter. Based on the numerical results, we have got the most possible form of the function on the right hand side of eq 15, which could be the power function of the Weber number and the dimensionless neck diameter d^*. According to eq 10, the breaking time can be written as

$$t_n = a_2(We^{\alpha_1}\cdot d^{*\alpha_2}) + c_2$$

$$= a_2[We^{\alpha_1}\cdot(a_1 We^{b_1} + c_1)]^{\alpha_2} + c_2 \tag{16}$$

When the Weber number is small (i.e., $We < 0.5$ in present work), we can only keep the lowest order of We. At last, the droplet breaking time can be predicted with the Weber number as

$$t_b \approx t_n = aWe^b + c \tag{17}$$

where $a = 0.29$, $b = -0.2$, and $c = -0.15$.

5. CONCLUSIONS

(1) The evolution of the gas−liquid interface during the formation process of the droplet was captured numerically and experimentally as the glycerol mass fraction is 50%, and both results are well in agreement with each other.

(2) The droplet formation can be divided into three stages: forming stage, necking stage, and breaking stage. As the droplet growing, a clockwise vortex in the droplet is formed. The increasing gravity causes the vortex to become larger, and then, the neck phenomenon occurs. At the breaking time, the relative velocity differences stretch and shrink the neck and finally cause the breakup.

(3) When $We < 0.05$, the length and volume of the droplet increase, and the breaking time decreases rapidly. On the other side, when $We > 0.05$, the flow rate has little effect on droplet geometric parameters.

(4) The resultant force suddenly drops around the critical time for the droplet to breakup. The difference rate between the time t_n (when the resultant force is zero) and the breaking time t_b increases from 0.15 to 8.49%; therefore, the t_n is approximately equal to t_b.

(5) The approximate formula of droplet neck diameter is determined, as shown in eq 10.

(6) After the force and dimensional analysis, combined with the numerical results, the prediction formula of breaking time on the Weber number is determined, as shown in eq 17, for $We < 0.5$.

AUTHOR INFORMATION

Corresponding Author

Peifeng Lin − *Key Laboratory of Fluid Transmission Technology of Zhejiang Province, Zhejiang Sci-Tech University, Hangzhou 310018, China;* orcid.org/0000-0001-8089-2376; Email: linpf@zstu.edu.cn

Authors

Qi Chen − *Key Laboratory of Fluid Transmission Technology of Zhejiang Province, Zhejiang Sci-Tech University, Hangzhou 310018, China*

Youju Liu − *Key Laboratory of Fluid Transmission Technology of Zhejiang Province, Zhejiang Sci-Tech University, Hangzhou 310018, China*

Xiao Hu − *Key Laboratory of Fluid Transmission Technology of Zhejiang Province, Zhejiang Sci-Tech University, Hangzhou 310018, China*

Zuchao Zhu − *Key Laboratory of Fluid Transmission Technology of Zhejiang Province, Zhejiang Sci-Tech University, Hangzhou 310018, China*

Complete contact information is available at: https://pubs.acs.org/10.1021/acsomega.2c02602

Notes

The authors declare no competing financial interest.

ACKNOWLEDGMENTS

The present work is financially supported by the Key R&D Program of Zhejiang Province (grant no. 2020C03081), the Joint Funds of the National Natural Science Foundation of China (grant no. U2006221), the Natural Science Foundation of Zhejiang province (grant no. LQ22A020008), and the National Natural Science Foundation of China (grant no. 51676173). The supports are gratefully acknowledged.

REFERENCES

(1) Nazari, A.; Zadkazemi Derakhshi, A.; Nazari, A.; Firoozabadi, B. Drop formation from a capillary tube: Comparison of different bulk fluid on Newtonian drops and formation of Newtonian and non-Newtonian drops in air using image processing. *Int. J. Heat Mass Transfer* **2018**, *124*, 912−919.

(2) Wang, T.; Jian, L.; Lei, Y.; Guo, X.; Fu, H. Droplets generator: Formation and control of main and satellite droplets. *Colloids Surf., A* **2018**, *558*, 303−312.

(3) Liu, S.; Liang, G.; Li, C.; Zhang, L.; Che, J.; Shen, S. The falling, necking, and break-up of droplet between horizontal tubes with low Reynolds number. *Int. J. Multiphase Flow* **2021**, *142*, 103717.

https://doi.org/10.1021/acsomega.2c02602
ACS Omega 2022, 7, 23890−23898

(4) Brenner, M. P.; Eggers, J.; Joseph, K.; Nagel, S. R.; Shi, X. D. Breakdown of scaling in droplet fission at high Reynolds number. *Phys. Fluids* **1997**, *9*, 1573−1590.
(5) Nazari, A.; Nazari, A. Experimental Investigation on Newtonian Drop Formation in Different Continuous Phase Fluids. In *ASME 2018 International Mechanical Engineering Congress and Exposition*; American Society of Mechanical Engineers: Pittsburgh, Pennsylvania, USA, 2018.
(6) Hu, X.; Lin, P.; Lin, J.; Zhu, Z.; Yu, Z. On the polydisperse particle migration and formation of chains in a square channel flow of non-Newtonian fluids. *J. Fluid Mech.* **2022**, *936*, A5.
(7) Tang, Z.; Fang, K.; Bukhari, M. N.; Song, Y.; Zhang, K. Effects of Viscosity and Surface Tension of a Reactive Dye Ink on Droplet Formation. *Langmuir* **2020**, *36*, 9481−9488.
(8) Dastyar, P.; Salehi, M. S.; Firoozabadi, B.; Afshin, H. Experimental investigation of the effects of surfactant on the dynamics of formation process of liquid drops. *J. Ind. Eng. Chem.* **2020**, *89*, 183−193.
(9) Dong, H.; Carr, W. W.; Morris, J. F. An experimental study of drop-on-demand drop formation. *Phys. Fluids* **2006**, *18*, 072102.
(10) Zhang, X.; Basaran, O. A. An experimental study of dynamics of drop formation. *Phys. Fluids* **1995**, *7*, 1184−1203.
(11) Viswanathan, H. Breakup and coalescence of drops during transition from dripping to jetting in a Newtonian fluid. *Int. J. Multiphase Flow* **2019**, *112*, 269−285.
(12) Ambravaneswaran, B.; Wilkes, E. D.; Basaran, O. A. Drop formation from a capillary tube: Comparison of one-dimensional and two-dimensional analyses and occurrence of satellite drops. *Phys. Fluids* **2002**, *14*, 2606−2621.
(13) Eggers, J.; Dupont, T. F. Drop Formation in a One-Dimensional Approximation of the Navier-Stokes Equation. *J. Fluid Mech.* **1994**, *262*, 205−221.
(14) Subramani, H. J.; Yeoh, H. K.; Suryo, R.; Qi, X.; Basaran, O. A. Simplicity and complexity in a dripping faucet. *Phys. Fluids* **2006**, *18*, 032106.
(15) Xu, Q.; Basaran, O. A. Computational analysis of drop-on-demand drop formation. *Phys. Fluids* **2007**, *19*, 102111.
(16) Fawehinmi, O. B.; Gaskell, P. H.; Jimack, P. K.; Kapur, N.; Thompson, H. M. A combined experimental and computational fluid dynamics analysis of the dynamics of drop formation. *Proc. Inst. Mech. Eng., Part C* **2005**, *219*, 933−947.
(17) Mao, X.; Zhang, L.; Zhao, Z.; Lin, F. Generation of droplets via oscillations of a tapered capillary tube filled with low-viscosity liquids. *Phys. Fluids* **2017**, *29*, 067104.
(18) Karbaschi, M.; Taeibi Rahni, M.; Javadi, A.; Cronan, C. L.; Schano, K. H.; Faraji, S.; Won, J. Y.; Ferri, J. K.; Krägel, J.; Miller, R. Dynamics of drops—Formation, growth, oscillation, detachment, and coalescence. *Adv. Colloid Interface Sci.* **2015**, *222*, 413−424.
(19) Pandey, V.; Deka, H.; Biswas, G.; Dalal, A. Dynamics of Growth and Breakup of an Evaporating Pendant Drop. *J. Heat Transfer* **2020**, *142* (2), 21601.
(20) Zhang, Y.; Zhu, H.; Zhu, J.; Shi, Q.; Valdivieso, A. L. Characteristic evolution and energy variation during the generation of kerosene droplet. *Fuel* **2021**, *288*, 119684.
(21) Majumder, A.; Ghosh, D.; Kumar Das, P. Dynamics of drop formation, growth and pinching phenomena from a submerged nozzle. *Chem. Eng. Sci.* **2021**, *245*, 116808.
(22) Yang, J.; Zheng, F.; Derby, B. Stability of Lines with Zero Receding Contact Angle Produced by Inkjet Printing at Small Drop Volume. *Langmuir* **2021**, *37*, 26−34.
(23) Wang, Z.; Zhang, Y.; Li, R.; Wang, Q.; Wang, J. An experimental study on drop formation from a capillary tube. *J. Braz. Soc. Mech. Sci. Eng.* **2020**, *42*, 110.
(24) Youngsd, D. L. *Time-dependent multi-material flow with large fluid distortion*; Academic Press, 1982.
(25) Barhate, R. S.; Patil, G.; Srinivas, N. D.; Raghavarao, K. S. M. S. Drop formation in aqueous two-phase systems. *J. Chromatogr. A* **2004**, *1023*, 197−206.
(26) Heertjes, P. M.; de Nie, L. H.; de Vries, H. J. Drop formation in liquid-liquid systems-I prediction of drop volumes at moderate speed of formation. *Chem. Eng. Sci.* **1971**, *26*, 441−449.
(27) Wei, W.; Ngan, K. H.; Jing, G.; Angeli, P. Observations on single drop formation from a capillary tube at low flow rates. *Colloids Surf., A* **2009**, *334*, 197−202.
(28) Byakova, A. V.; Gnyloskurenko, S. V.; Nakamura, T.; Raychenko, O. I. Influence of wetting conditions on bubble formation at orifice in an inviscid liquid - Mechanism of bubble evolution. *Colloids Surf., A* **2003**, *229*, 19−32.

https://doi.org/10.1021/acsomega.2c02602
ACS Omega 2022, 7, 23890−23898